Journal of Materials Chemistry A

ROYAL SOCIETY OF CHEMISTRY

PAPER

View Article Online
View Journal | View Issue

Cite this: J. Mater. Chem. A, 2025, 13, 11886

Transparent nature-based luminescent solar concentrator with NIR emission and integrated thermal sensing†

Sandra F. H. Correia, *[a] Bruno P. Falcão, ‡[b] Gonçalo Figueiredo, [bc] Bárbara M. C. Vaz,[d] Letícia S. Contieri,[de] Leonardo M. de Souza Mesquita, [de] Juliana Almeida,[fg] Joana C. Fradinho, [fg] Diana C. G. A. Pinto, [h] Lianshe Fu, [b] Paulo S. André,[c] Sónia P. M. Ventura, [d] Rute A. S. Ferreira [b] and Vitor Sencadas*[i]

The engineering of luminescent solar concentrators (LSCs) offers a way to turn windows into energy-generating units while maintaining transparency. Through UV/blue down-shifting materials to the red/near-infrared (NIR) spectral region, the performance of building integrated photovoltaics is maximized without compromising indoor light quality. The most efficient solutions are based on quantum dots, which raise environmental concerns. To address this, natural renewable materials, like bacteriochlorophyll (BChl) from phototrophic bacteria were used to fabricate an LSC prototype dispersed in a styrene–ethylene–butylene–styrene (SEBS) matrix. The LSCs emit in the red/NIR region with an emission quantum yield of ~7%, demonstrating external photon efficiency and electrical device efficiency values of ~1.0% and ~0.04%, respectively. The thermal dependence of the BChl/SEBS emission is used to set two independent thermometric parameters based on the emission and the electrical power generated by the LSC edge-mounted photovoltaic cells with relative sensitivity values up to ~2% °C^{-1}, which is a remarkable performance. This prototype was scaled up for an active area of 0.1 m^2, representing the first large-area LSC using nature-based red/NIR emission centers.

Received 12th November 2024
Accepted 19th March 2025

DOI: 10.1039/d4ta08036j

rsc.li/materials-a

Introduction

Three primary sectors—buildings, industry, and transportation—are global energy consumers, with buildings leading the consumption. Windows, a significant factor in heat dynamics, offer potential for energy transformation *via* luminescent solar concentrators (LSCs).[1,2] Developing efficient LSC transparent devices for natural lighting and energy harvesting requires UV-absorbing and NIR-emitting centers.[3,4] However, these centers are scarce and mostly reliant on quantum dots (QDs), which involve complex processing and present significant environmental risks, primarily related to toxicity *via* aquatic organisms and bioaccumulation.[5,6] Meeting Sustainable Development Goals (SDG 7 and 9 affordable and clean energy; and industry, innovation, and infrastructure, respectively)[7] demands innovative, efficient LSCs capable of broad solar radiation absorption, minimal re-absorption, and emission compatible with Si-based commercial photovoltaic (PV) cells.

In response to these challenges, the spotlight is shifting towards natural molecules, offering a sustainable alternative for LSCs.[8–12] Furthermore, cutting-edge developments in LSC technology now incorporate sensing capabilities, enabling these devices to function as sunlight-powered optical temperature

[a]Instituto de Telecomunicações, University of Aveiro, Campus Universitário de Santiago, 3810-193 Aveiro, Portugal. E-mail: sandracorreia@av.it.pt
[b]Department of Physics, CICECO – Aveiro Institute of Materials, University of Aveiro, 3810-193 Aveiro, Portugal
[c]Department of Electrical and Computer Engineering, Instituto de Telecomunicações, Instituto Superior Técnico, University of Lisbon, 1049-001 Lisbon, Portugal
[d]Department of Chemistry, CICECO – Aveiro Institute of Materials, University of Aveiro, 3810-193 Aveiro, Portugal
[e]Multidisciplinary Laboratory of Food and Health (LabMAS), School of Applied Sciences (FCA), University of Campinas, Rua Pedro Zaccaria 1300, Limeira, Sao Paulo, 13484-350, Brazil
[f]Associate Laboratory i4HB – Institute for Health and Bioeconomy, NOVA School of Science and Technology, NOVA University of Lisbon, 2829-516 Caparica, Portugal
[g]UCIBIO – Applied Molecular Biosciences Unit, Department of Chemistry, NOVA School of Science and Technology, NOVA University Lisbon, 2829-516 Caparica, Portugal
[h]LAQV – REQUIMTE, Department of Chemistry, University of Aveiro, 3810-193 Aveiro, Portugal
[i]Department of Materials and Ceramic Engineering, CICECO – Aveiro Institute of Materials, University of Aveiro, 3810-193 Aveiro, Portugal. E-mail: vsencadas@ua.pt

† Electronic supplementary information (ESI) available. See DOI: https://doi.org/10.1039/d4ta08036j

‡ Present address: i3N and Department of Physics, University of Aveiro, 3810-193 Aveiro, Portugal.

sensors integrated with IoT networks.[13–16] This integration enhances LSC functionality and drives the advancement of smart, energy-efficient building technologies. By harnessing renewable energy and providing critical environmental data, natural molecules play a pivotal role in the future of LSCs, marking a significant leap towards sustainable energy solutions like supply-less IoT-based windows.[15]

Theoretical studies have shown the potential of NIR-emitting LSCs using QDs,[17–21] indicating an external photon efficiency (η_{ext}, defined as the ratio between the output and input optical power) of up to 14.6%,[18] however, few experimental reports quantify the performance of planar NIR-based LSCs.[8] These LSCs, using optically active layers with PbS,[22,23] PbSe,[24] PbS/CdS,[25] CISeS/ZnS,[6] CZISe/ZSe,[26] $CuInS_2$,[27] $CuInS_2$/ZnS,[28] $CuInS_2$/Zn/Al,[29] and Si QDs,[30] or synthetic dyes[31–34] or even nanocrystals[35] typically show η_{ext} values below 8.1%[28] (for single edge collection), correspondent to a device efficiency (η_{dev}, defined as the ratio between the output electrical power and the incident optical power) of 2.18%.[28] Higher values, up to 12.6%, when considering all edges in a planar LSC,[23] have been reported, both using PbS QDs. To address QDs' limitations—lower quantum yield in the NIR range, toxicity, and photoblinking—alternative NIR-emitting LSCs based on hexanuclear metal halide clusters[3] and a cyanine derivative[4] have been explored without quantitative performance characterization. The performance of a NIR-emitting LSC based on silicon 2,3-naphthalocyanine bis(trihexylsilyloxide) (SiNc) immobilized in an organic–inorganic triureasil matrix t-U(5000) and coupled to a Si-based PV device revealed $\eta_{ext} \sim 1.5\%$.[34]

Recent studies emphasize the potential of natural renewable materials in LSCs,[9–13,36–38] aligning with the growing demand for natural products across various sectors.[39] Addressing environmental impact concerns in industries has heightened the push for sustainability. Integrating natural materials into smart, low-waste manufacturing chains aligns with current sustainability concepts. While some LSCs based on natural molecules have emerged,[10–13,36–38] none emit in the red/NIR spectral range, vital for maximum absorption by c-Si PV cells. This highlights the need for the search of new nature-derived red/NIR-emitting materials to boost LSC sustainability without compromising efficiency.

Ensuring the photostability and processability of films of bio-based materials is critical alongside optical performance.[9] Styrene–ethylene–butylene–styrene (SEBS) emerges as a notable thermoplastic elastomer suitable for smart windows.[15] It has polystyrene (hard PS block) at both ends and poly(ethylene-*co*-1-butene) (soft PEB block) in the middle.[40] Its processability, transparency, cost-effectiveness and thermal behavior (glass transition temperature (T_g) of the hard-block around 100 °C),[41] that is similar to polymethylmethacrylate (PMMA, $T_g \approx 110$ °C),[42] a commonly used hosting matrix material for LSC applications, make it a viable alternative. Produced by hydrogenating styrene–butadiene–styrene copolymer, SEBS improves heat stability and weather resistance. Known for its rubber-like properties, high elasticity, and excellent tensile strength, SEBS is widely used in various applications requiring flexibility and durability, including automotive parts, adhesives, and roofing materials. Its high UV resistance[43] makes it an ideal choice for outdoor applications like windows, particularly in high-temperature environments.[44] Incorporating natural pigments such as bacteriochlorophylls (BChls) with photosynthetic potential, holds promise for smart, highly energy-efficient windows.[45]

BChl, found in photosynthetic bacteria, features a tetrapyrrole ring structure similar to chlorophylls (Chls) but with a more reduced ring, enabling light absorption at longer wavelengths.[46] While BChl does not produce oxygen like chlorophyll-containing organisms during light conversion, its unique ability for anoxygenic photosynthesis is valuable in low-light conditions, showing potential for high-performance energy materials.[47] These pigments notably harness light in UV and NIR spectral regions.[46] However, the traditional recovery of BChl often involves harmful solvents like acetone or methanol.[48–50] Replacing such solvents, especially methanol known for its hazards and lower efficiency, is crucial to reduce environmental and economic impact. Furthermore, the thermal dependence of the BChl optical properties allows the use of luminescence as a method for remote temperature measurement, capitalizing on the thermal dependency of phosphor emission. This innovative approach, initially tailored for conventional spectrometers, has been adapted to mobile optical (mOptical) sensing, leveraging the charge-coupled devices (CCDs) within smartphones and facilitating sensing functions.[51,52] Recent findings propose using the inherent temperature-dependent emission effects of LSCs, which cause variations in the electrical output of edge-coupled PV cells, as a basis for thermal sensing.[13–15] This work presents the development of a large-area LSC utilizing a nature-based NIR-emitting optically active material with temperature-sensing capabilities. It pioneers the use of a natural molecule emitting in the NIR spectrum for large-area LSC prototypes, where the cultivation of this molecule is a by-product of polyhydroxyalkanoate (PHA) production, thus aligning with the principles of biorefinery and resource optimization. Furthermore, the thermal dependence of the optical properties of BChl is leveraged to transform the LSC prototype into an *in situ*, sunlight-powered optical temperature sensor.[13–15]

Experimental

Materials and methods

Chemical compounds. Ethanol and acetone (HPLC grade), chloroform (Puriss Ph. Eur. 99.0–99.4% GC), dimethyl ether (99% purity), surfactants sodium dodecylsulfate (pharma grade) and polyethylene glycol sorbitan monolaurate (Tween 20), along with various ammonium bromides, were obtained from multiple suppliers including Fisher Scientific, Sigma-Aldrich, Panreac, Carlo Erba, Alfa Aesar, Tokyo Chemical Industry, IoLiTec, and Honeywell. SEBS (Calprene H6180X, with 85/15 ethylene butylene/styrene ratio) was kindly supplied by Dynasol Group (ESI† for details).

Phototrophic mixed cultures operation. Activated sludge from Beirolas wastewater treatment plant in Lisbon (Portugal) was enriched with phototrophic purple bacteria under 24 hour cycles in a 4.2 L sequencing batch reactor (SBR) at 30 °C. The

phototrophic mixed culture (PMC) was cultivated with continuous illumination from four halogen lamps, emitting light at 90.9 W m^{-2} and limiting input to NIR wavelengths using a UV-visible absorbing filter (Lee Colour Filter 299 1.2 N.D.). The reactor received synthetic solutions of butyric acid, mineral medium, and phosphate medium. Inorganic carbon feeding occurred twice in the cycle, pH was controlled at 6.5 using HCl (1 M) and NaOH (1 M), and the reactor operated with hydraulic retention time (HRT) and solids retention time (SRT) of 3 days. The biomass used for this study was freshly collected from the 1.4 L withdrawal of the reactor and centrifuged at 10 000*g*, for 30 minutes at room temperature. The supernatant was discharged, and the biomass pellets were stored at −20 °C until further processing. The biomass collection occurred for 2 weeks until 10 g of biomass was recovered. This process is represented in Fig. 1a.

BChl extraction. Several solvents were used and their performance in the extraction of BChl was studied. Included in the set of solvents, different organic solvents (aqueous ethanol at 50% (v/v) and pure ethanol, acetone, and dimethyl ether), water, some tension-active cationic ionic liquids, and anionic, and non-ionic aqueous solutions of surfactants at 250 mM were investigated. The selection of the solvents to use was based on previous knowledge of the extraction of Chls.[53–56] The extraction process involved shaking using a digital shaker at room temperature for 30 minutes, followed by centrifugation at 4700*g* for 30 minutes at 4 °C. The supernatant containing BChl was collected, and solvent removal was achieved using a rotary evaporator to obtain dry BChl for further use. Quantification was performed by UV-visible absorption spectra (Fig. S1, ESI†) analysis using a microplate reader, and extraction efficiency was calculated based on the best solvent's absorption peaks at 775 nm for organic solvents and 757 nm for aqueous solutions of tension-active compounds. This process is represented in Fig. 1a.

Identification of the pigments by UHPLC-MS/MS. BChl ethanolic and sodium dodecyl sulfate (SDS) extracts underwent UHPLC-MS/MS analysis using a Thermo Scientific Ultimate 3000RSLC system coupled to a mass spectrometer. The analysis was conducted in positive mode, employing a gradient elution program on a Hypersil Gold C18 column (100 × 2.1 mm i.d.; 1.9 μm particle diameter, Thermo Fisher) at a flow rate of 2 mL min^{-1} and 30 °C. The mobile phase comprised 0.1% formic acid in water (A) and a mixture of acetonitrile (30) and methanol (70) (B), with a 5 μL injection volume into the UHPLC system.

Incorporation of BChl into SEBS matrix. The SEBS elastomer was dissolved in chloroform (9.0 mL of solvent for 1.0 g of polymer) using a magnetic stirrer (MST, VELP). After complete dissolution, the solution was poured into a glass Petri dish and left to evaporate overnight at room temperature. For BChl/SEBS samples, various amounts of dried BChl (2, 6, 10, and 20 wt%) were suspended in chloroform, followed by addition of SEBS and complete dissolution using a magnetic stirrer. The BChl/SEBS films were obtained following the same process as the pure SEBS matrix. Optical characterization was performed on samples denoted as BChl/SEBS-*X* (*X* = 1, 2, 3, 4) prepared with different concentrations of 2, 6, 10, and 20 wt%, respectively. This process is represented in Fig. 1b.

Fabrication of the LSC device. After analysis of the optical features of each sample, the BChl/SEBS-2 material was selected and deposited on a glass substrate (dimensions 10.5 × 10.5 × 0.8 cm^3) using the doctor-blade deposition method (Automatic

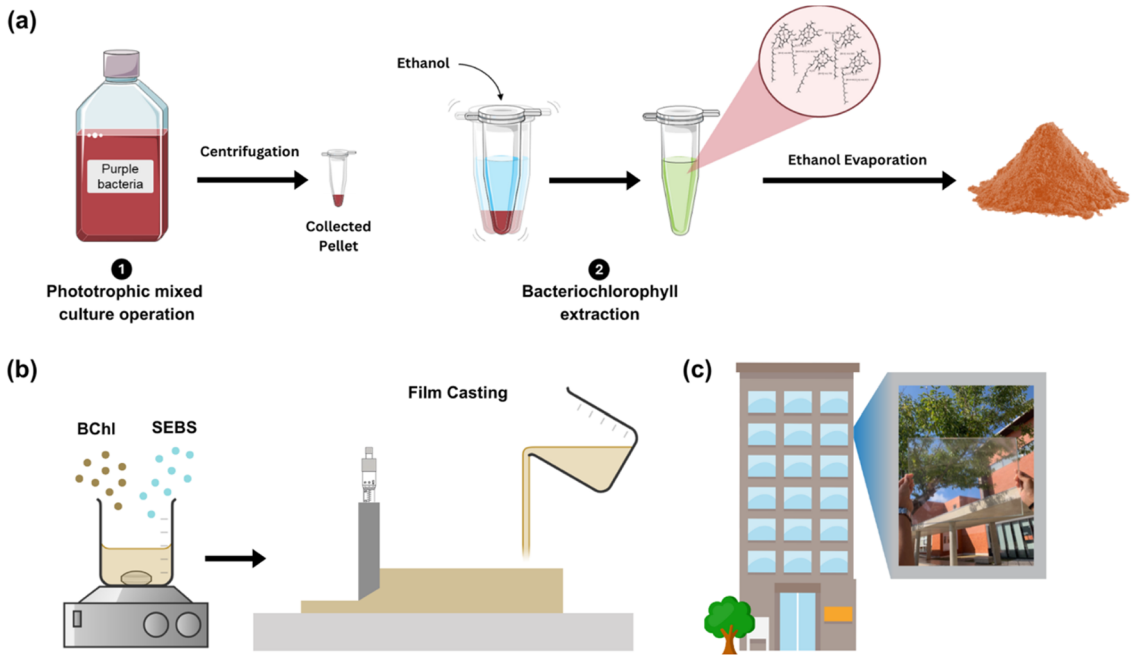

Fig. 1 Schematic representation of the experimental steps concerning (a) phototrophic mixed cultures operation and BChl extraction, (b) the incorporation of BChl into SEBS matrix and film deposition. (c) Schematic representation of the building integrated LSCs with a photograph of the fabricated device.

Film Applicator AB4400, TQCSheen) and the solvent was allowed to evaporate at room temperature. The thickness of the films was measured using an optical profilometer (Profilm3D®, Filmetrics, Fig. S2, ESI†), yielding values of 10.51 ± 0.01 μm. The LSC window prototypes were framed in polyvinyl chloride (PVC) and incorporated an array of 12 series-connected c-Si solar cells (IXOLAR™ SolarBITs, ANYSOLAR, KXOB25-01X8F). The solar cells were mechanically coupled, without the use of any glue, to collect light on three of the prototype's four sides. The BChl/SEBS-2 sample was also deposited on large-area glass substrates (28 × 38 × 0.8 cm^3, Fig. 1c) using the previously mentioned deposition method. In this case, the solar cells (IXOLAR, SM281K07 TF) were coupled only on the longer edges of the LSC.

Structural and thermal characterization. Infrared spectroscopy (FT-IR) using the attenuated total reflectance (ATR) mode (Tensor 27, Bruker) analyzed the sample spectra within 4000–400 cm^{-1}, at a resolution of 4 cm^{-1} with 256 scans. Scanning electron microscopy (SEM, SU70, Hitachi) assessed sample morphology after coating with an Au–Pd thin layer *via* sputtering (E5000, Polaron). Thermal stability was determined through thermogravimetry (TGA, STA 300, Hitachi) in the range of 40–800 °C, at a heating rate of 20 °C min^{-1} and differential scanning analysis (DSC, 300 Caliris, Netzsch) at 10 °C min^{-1}, both under a nitrogen atmosphere. BChl powder was obtained by evaporation of the solvent in BChl ethanolic solution and used for X-ray diffraction (XRD) measurement. XRD patterns were collected on a PANalytical Empyrean X-ray Diffractometer operating at 45 kV and 40 mA, with Cu Kα radiation at 1.5406 Å in the 2θ range of 3°–60°. Sample surface characterization was determined by AFM imaging (FX40 AFM, Park Systems). Imaging was performed in PointProbe Plus Non-Contact Mode High Resonance Frequency (PPP-NCHR) with a doped silicon probe (NANOSENSORS). The probe had a spring constant of 10 N m^{-1}, resonant frequency of 325.1 kHz, nominal tip height of 5–10 nm, and cantilever length of 125 μm. The Park SmartAnalysis (Park Systems) was used to analyze the AFM images and calculate the roughness parameter values for each sample. The mechanical characterization was performed at room temperature, in the tensile mode at a stroke speed of 10 mm min^{-1} using a universal testing machine (EZ-LX, from Shimadzu) fitted with a 10 N load cell. The results are presented as the average ± standard deviation of six different specimens for each sample.

Optical characterization. UV-visible transmittance spectra of the BChl/SEBS films were obtained using a Lambda 950 dual-beam spectrometer (PerkinElmer). Photoluminescence spectra were captured with a modular double-grating excitation spectrofluorimeter (Fluorolog-3, Horiba Scientific) connected to an R928 Hamamatsu photomultiplier. Emission decay curves were recorded at room temperature using a Fluorolog TCSPC spectrofluorometer (Horiba Scientific) with a 200 × 10^{-9} s time-to-amplitude converter. Absolute emission quantum yield (q) values were measured at room temperature through a C9920-02 Hamamatsu system. Photostability of the BChl/SEBS samples was evaluated after being placed inside a climatic chamber (Angelantoni Industrie, Model Challenge 340) subjected to distinct test conditions at constant temperature (T) and relative humidity (RH) values, namely, T = 25.0 °C/RH = 95%; T = 50.0 °C/RH = 60%. The accuracy is 0.3 °C and 3%, respectively, with each test having the duration of 24 h. The emission spectra were measured with the spectrofluorimeter and integrating sphere above mentioned for the measurement of the photoluminescence and emission quantum yield, respectively.

Electrical characterization. The prototypes' *I–V* characteristics were assessed under simulated solar radiation (OSRAM Ultra-Vitalux 300 W, ~225 W m^{-2}) using a Keithley 2400 series source meter unit. The incident optical power was measured using a calibrated reference solar cell and meter (91150V, Newport). To ensure reliability, measurements were repeated at least three times, with the associated error corresponding to the standard deviation among distinct measurements.

Temperature-dependent measurements. Temperature-dependent *I–V* measurements under AM 1.5 G illumination were performed in the temperature range of 25–45 °C. Simultaneously, the emission spectra were recorded at the edge of the LSC using an optical fiber connected to a portable spectrometer (SensLine, AVANTES, slit 100 μm) for real-time acquisition. All measurements were carried out in a homemade setup comprising a temperature-controlled hotplate, a thermocouple sensor to monitor the local temperature of the prototypes, and a Keithley 2400 series source meter to record the *I–V* values with an accuracy of 10^{-10} A and 10^{-4} V, respectively. In this case, to have a calibration curve independent of the power fluctuations of the light source, the thermometric parameter (Δ) values were normalized to the ones at 25 °C. The figures of merit to evaluate the performance of the thermometers are the sensitivity, S_r, and the temperature uncertainty, δT, defined as:[57,58]

$$S_r = \frac{1}{\Delta}\left|\frac{\partial \Delta}{\partial T}\right| \quad (1)$$

and

$$\delta T = \frac{1}{S_r}\frac{\delta \Delta}{\Delta} \quad (2)$$

where $\delta\Delta$ is the uncertainty in the determination of the thermometric parameter Δ. We note that, according to the manufacturer, the thermal dependence of the bare PV cells generating power is very low (<1%) in the considered temperature range.[59]

Results and discussion

BChl extraction

The structure of Chls comprises a hydrophobic phytol tail, yet it possesses polar functionalities due to C–O and C–N bonds, along with a chelated magnesium ion, mirroring BChl's structural traits.[60] Various solvents were tested (Fig. 2a) to evaluate their effectiveness in extracting BChl, with solvent polarity playing a crucial role in influencing the recovery of BChl, evident in Fig. 2b: high-polarity solvents like water and aqueous ethanol (50% v/v), along with low-polarity solvents like dimethyl ether, showed lower performance. Ethanol and acetone, owing to both their polarity and cell membrane disruption capability,

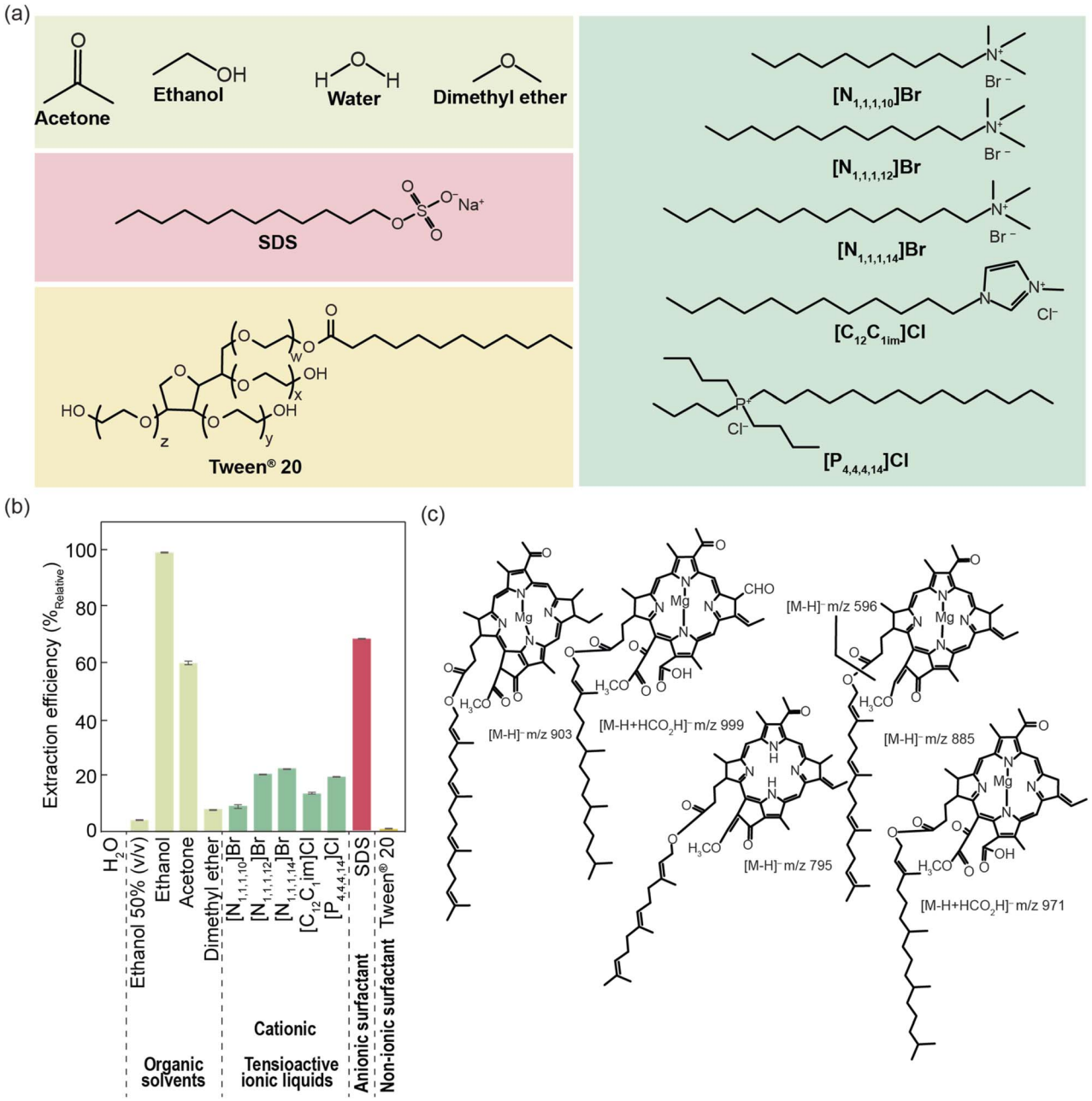

Fig. 2 (a) Molecular structures and abbreviation names of the solvents tested on the extraction of BChl. (b) BChl extraction efficiency with distinct solvents. (c) Chemical structures of the BChls identified by UHPLC-MS/MS analysis.

demonstrated improved extraction efficiency.[61] Furthermore, the impact of different classes of surface-active compounds on BChl release was evaluated. Tension-active compounds, particularly cationic ones, facilitated cell membrane disruption by interacting with phospholipids, with longer alkyl chains showing slightly better extraction efficiency.[62,63] Anionic compounds generally had limited effectiveness, except for SDS,[53,54] which stood out by enhancing Chl and BChl extraction.[53,54] Among the alternative solvents tested, SDS exhibited the highest extraction efficiency, reaching approximately 70-$\%_{relative}$, surpassing acetone (around 60$\%_{relative}$). Both SDS and ethanol extracts were analyzed, confirming the presence of Chl, BChl, and various derivatives (Fig. 2c and Tables S1–S3, ESI†). Considering the goal of maximizing pigment content for better film performance in LSCs, ethanol, as a less hazardous solvent, was chosen for further developments.

Structural and thermal properties

The films of SEBS with different BChl concentrations (denoted as BChl/SEBS-*X*, where $X = 1, 2, 3, 4$ according to the BChl concentration of 2, 6, 10, and 20 wt%, respectively) present high flexibility (Fig. 3a), exhibiting a consistently smooth morphology (average roughness below 69 nm) across different

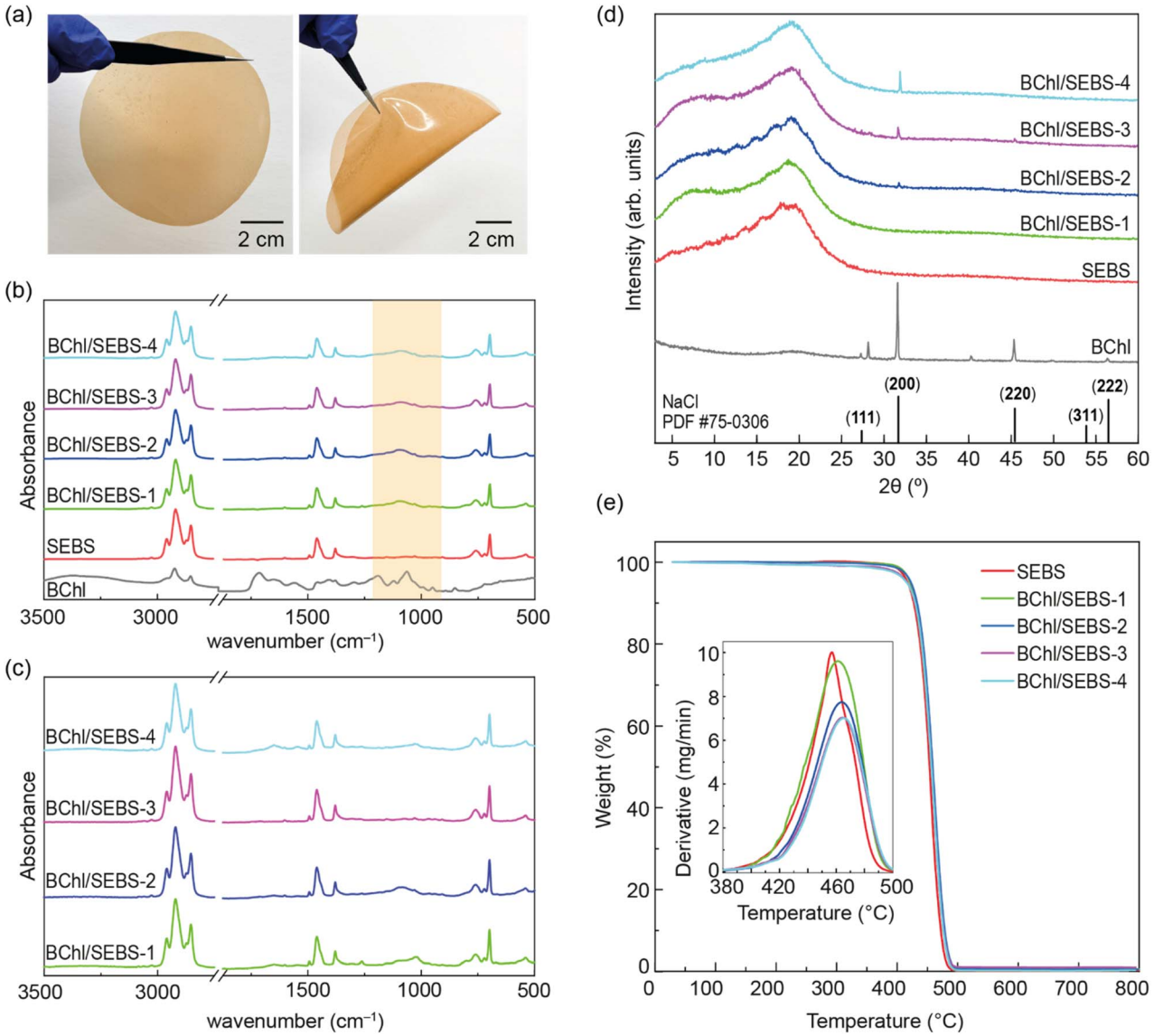

Fig. 3 (a) Photographs of BChl/SEBS-4 free standing film showing the flexibility of the material. FT-IR spectra of BChl/SEBS materials (b) before and (c) after exposition to AM 1.5 G radiation. The data for the BChl extract and undoped SEBS matrix are also presented. (d) XRD patterns of BChl, SEBS and BChl/SEBS samples. (e) Thermogravimetric analysis of the BChl/SEBS samples and of the undoped SEBS matrix.

BChl amounts (Fig. S3, ESI†). FT-IR spectra of the SEBS matrix, BChl solid extract, and BChl/SEBS composites pre and post AM 1.5 G solar radiation exposure are shown in Fig. 3b and c. For SEBS, absorption bands were observed at 2960 and 2923 cm^{-1} that are attributed to C–H asymmetric stretching of $–CH_3$ (in PEB block) and $–CH_2–$ (in PEB block and PS block), respectively, and an absorption band at 2852 cm^{-1} that is associated with C–H symmetric stretching of $–CH_2–$ in both PEB block and PS block.[40] Bands at 1460 and 1379 cm^{-1} are the C–H bending of $–CH_2–$ and $–CH_3$ in PEB block, respectively. Bands at 760 and 698 cm^{-1} are due to =C–H bending vibrating of side benzene ring in PS block, whereas the weak band at 721 cm^{-1} is from C–H rocking of $–CH_2–$ in PEB block. For BChl, bands at 2956 and 2923 cm^{-1} indicate $–CH_3$ and $–CH_2–$ asymmetric stretching vibrations, respectively, while the band at 2854 cm^{-1} is from symmetric stretching vibration of $–CH_2–$. The strong bands located at 1720 and 1650 cm^{-1} can be assigned to the C=O vibrations of the BChl molecule at different positions.[64] Bands at 1190 and 1060 cm^{-1} tentatively relate to Chl's C–N absorption,[65] which can also be discerned in the spectra of BChl/SEBS composites, indicating that BChl was encapsulated into SEBS. Remarkably, no perceptible changes were evident in the FT-IR spectra post-irradiation (Fig. 3c), suggesting that the main chemical structure remains unaffected.

The XRD patterns of BChl, SEBS and BChl/SEBS samples are presented in Fig. 3d. The XRD pattern of BChl shows a weak broad band centered at 2θ of 20°, indicating that BChl is in an amorphous state. The sharp peaks located at 27.3, 31.6, 45.3, and 56.4° are associated with NaCl, matching well the NaCl reference (JCPDS card no. 75-0306), suggesting that some NaCl

remained from the mineral medium used in PMC. The XRD pattern of SEBS displays a broad band centered at 18.8° with some small diffraction peaks, corresponding to monoclinic crystals (α-form).[66] After incorporation of BChl into SEBS, the main diffraction profile is from the host SEBS, which implies that there are no significant changes of BChl doping on the XRD pattern. The weak sharp peaks are attributed to the NaCl from the medium using in the PMC to extract the BChl.

To investigate the thermal stability of SEBS and BChl/SEBS composites, thermogravimetric studies were performed (Fig. 3e). This analysis reveals that SEBS and BChl/SEBS composites are stable up to 400 °C, followed by gradual degradation culminating at 500 °C, displaying consistent maximum degradation temperatures without residual char formation. To evaluate the stabilization effect of SEBS on BChl, the TGA derivative (DTG) is used to investigate thermal stability, as the peaks of DTG curves can indicate the temperatures at which the maximum change of weight loss occurs.[67] The positions of the peaks in DTG curves are 456, 462, 464, 465 and 466 °C for SEBS and BChl/SEBS-*X* ($X = 1$, 2, 3 and 4), respectively (Fig. 3e), the same tendency as $T_{50\%}$ values ($T_{50\%}$ is defined as the temperature at which 50% of mass loss occurs) of 454, 456, 458, 459 and 460 °C for SEBS and BChl/SEBS-*X* ($X = 1$, 2, 3 and 4), respectively. Also, there is no significant difference in the elastic modulus between the pure SEBS matrix and the BChl/SEBS sample (Fig. S4 in ESI†), which are 1.1 ± 0.1 MPa and 1.2 ± 0.1 MPa, respectively. These results indicate that compared to the stability of SEBS, the encapsulation of BChl into SEBS is not detrimental to the stability of the BChl/SEBS composites, a behavior akin to SEBS nanocomposites with graphene nanoplatelets prepared *via* a melting-blending process.[68]

Optical properties

The BChl/SEBS samples presented a reddish coloration under UV irradiation, corresponding to the emission spectra shown in Fig. 4a, whose energy is independent of the BChl concentration. For all the cases, the spectra show two prominent bands around 690 and 770 nm, which may be attributed to the presence of Chl and BChl from the extract, respectively. The excitation spectra were monitored on the more intense bands (Fig. 4b), showing two main components with peaks around 380 and 420 nm for all the BChl/SEBS samples, which are also present in the absorption spectra (Fig. 4c). These peaks were attributed to the presence of Chl (which typically have characteristic peaks around 415 and 670 nm) and carotenoids.[69]

Both emission and excitation spectra presented a red-shift related to those of the BChl in ethanolic solution (Fig. S5, ESI†), which is due to the polarization interaction between BChl and SEBS, as reported before for other luminescent molecules incorporated into organic–inorganic hybrids.[14,70,71]

The emission decay curves were investigated, revealing a single exponential behavior (Table 1 and Fig. S6–S9, ESI†), yielding values of 5.1 ± 0.5 ns which are like the ones found for the BChl in ethanolic solution (Table 1 and Fig. S10, ESI†), suggesting that BChl was dispersed in SEBS homogeneously and the local environment of the molecule is preserved after incorporation. The emission properties of the BChl/SEBS materials were further quantified by measuring q values (Table 1). The data produced suggest that the incorporation of BChl into the SEBS matrix did not induce a negative effect on the photon conversion efficiency of these materials, and in some cases was beneficial, with higher q values comparing to those found for the BChl ethanolic solution, with maximum values of 0.07 ± 0.01, further demonstrating the protective effect of SEBS on BChl due to the interaction between them. To assess the potential of BChl in ethanolic solution and BChl/SEBS materials for absorbing solar radiation, the overlap integral (O) between their absorption spectra and the solar irradiation (AM 1.5 G) was estimated (Table 1). The calculations revealed that the BChl/SEBS samples have the ability to absorb up to 18% of the solar photon flux on Earth (4.3×10^{21} photons per s per m^2).[34] The photostability of the BChl/SEBS films was evaluated by exposing them to continuous AM 1.5 G for ~27 h with periodic q values measurement, which showed that the variation is within the 10% experimental error providing strong evidence of the material photostability (Fig. S11, ESI†). Also, accelerated aging tests (given the intended application of these LSCs as windows) were performed in a climatic chamber showing that these samples are stable under extreme conditions (Fig. S12, S13 and Table S4, ESI†). Given these results, it is not expected that the LSC devices will undergo significant performance degradation due to environmental conditions over time. One of the main parameters to evaluate the suitability of BChl as an optically active material for large-area LSCs is the reabsorption evaluated by the overlap between its absorption and emission spectra. This may be evaluated by the modified overlap integral OI* defined by:[33,72]

$$\mathrm{OI}^* = \frac{\int_0^\infty A(\lambda)\mathrm{PL}^*(\lambda)\mathrm{d}\lambda}{\int_0^\infty \mathrm{PL}^*(\lambda)\mathrm{d}\lambda} \quad (3)$$

where $A(\lambda)$ is the absolute absorption spectrum and $\mathrm{PL}^*(\lambda)$ is the normalized emission spectrum of the optically active material. The OI* values found for the BChl/SEBS samples are of the same order of the ones found for synthetic dyes applied for transparent LSCs,[32,33] showing that this material is promising for the intended application.

The Average Visible Transmission (AVT) of the fabricated BChl/SEBS samples lies in the range between 73 and 95% (Table 1) making them suitable for window applications.[73,74] To quantify the color appearance of the planar LSCs and their effects on color perception, the transmitted light was also analyzed in terms of CIE 1931 color space diagram coordinates and Color Rendering Index (CRI) which evaluated the ability to accurately render the color of objects (Fig. 4d and S14, ESI†). The light transmitted through the BChl/SEBS films showed coordinates that are very close to ideal white light (0.33, 0.33) (Table 1) and the CRI values indicated minimal distortion of incoming sunlight, further supported by the Color Correlation Temperature (CCT) values of the transmitted light (Table 1), corresponding to warm/neutral light. This makes the material suitable for residential or commercial spaces, highlighting its high potential as solar windows. Based on the data described

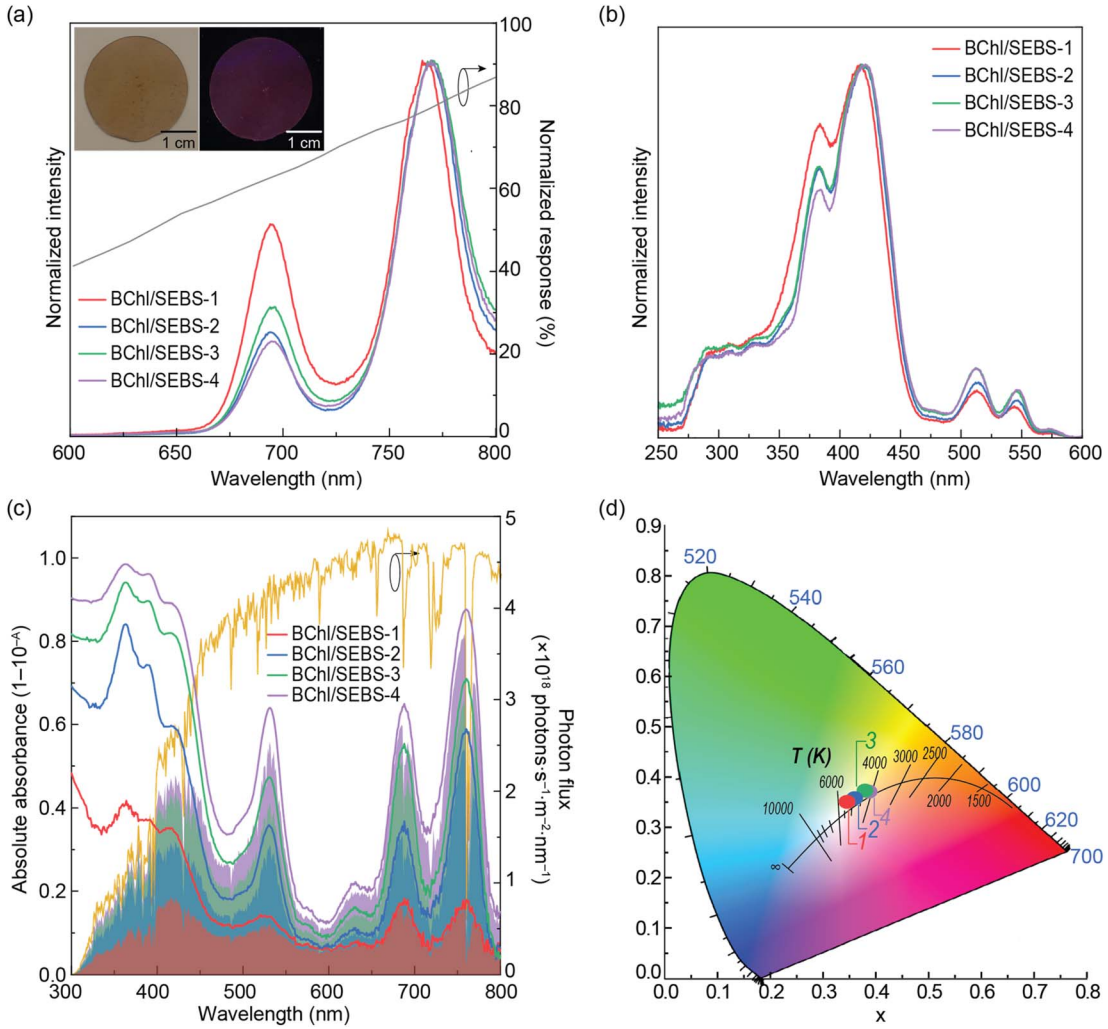

Fig. 4 (a) Emission spectra of BChl/SEBS samples excited at 360 nm. The grey line (right *y* axis) is the normalized c-Si absorption curve. The inset shows photographs of the BChl/SEBS-4 under indoor illumination (left) and UV radiation at 365 nm (right). (b) Excitation spectra of BChl/SEBS samples monitored at 695 nm. (c) Absorption spectra of BChl/SEBS samples. The right *y*-axis represents the AM 1.5 G photon flux, and the shaded area is the overlap integral *O*. (d) CIE 1931 colour space diagram showing colour coordinates of the transmitted light through BChl/SEBS-*X*, where $X = 1, 2, 3, 4$ under AM 1.5 G radiation.

above, namely the *O* and *q* values, and the quality of the transmitted light, the BChl/SEBS-2 sample was selected to be used in the fabrication of the LSC prototype.

Luminescent solar concentrator based on BChl/SEBS

A planar LSC was manufactured by coating a 10.5 × 10.5 × 0.8 cm^3 glass substrate and coupling it to an array of c-Si PV cells

Table 1 Overlap integral between absorption and AM 1.5 G spectra (*O*, photons per s per m^2) and between absorption and emission spectra (OI*), emission lifetime (τ, ns) and absolute emission quantum yield (*q*), for the BChl/SEBS samples. The color coordinates (*x*,*y*), color rendering index (CRI) and color correlated temperature (CCT) of the transmitted light of the BChl/SEBS samples under AM 1.5 G solar simulator and average light transmittance (AVT, %) are also presented

Sample	*O* (×10^{20} photons per s per m^2)	OI*	τ (ns)	*q*	(*x*,*y*)	CRI	CCT (K)	AVT (%)
BChl (ethanolic solution)	—	—	5.30 ± 0.01	0.03 ± 0.01[a]	—	—	—	—
BChl/SEBS-1	2.4	0.13	5.06 ± 0.04	0.07 ± 0.01[b]	(0.35,0.35)	95.3	4949	94.7
BChl/SEBS-2	4.4	0.35	5.58 ± 0.04	0.04 ± 0.01[c]	(0.36,0.36)	92.6	4455	87.6
BChl/SEBS-3	6.0	0.43	5.04 ± 0.03	0.04 ± 0.01[c]	(0.38,0.37)	89.2	3971	80.7
BChl/SEBS-4	7.9	0.60	4.74 ± 0.01	0.02 ± 0.01[c]	(0.39,0.37)	86.5	3750	72.6

[a] Excitation at 410 nm. [b] Excitation at 415 nm. [c] Excitation at 420 nm.

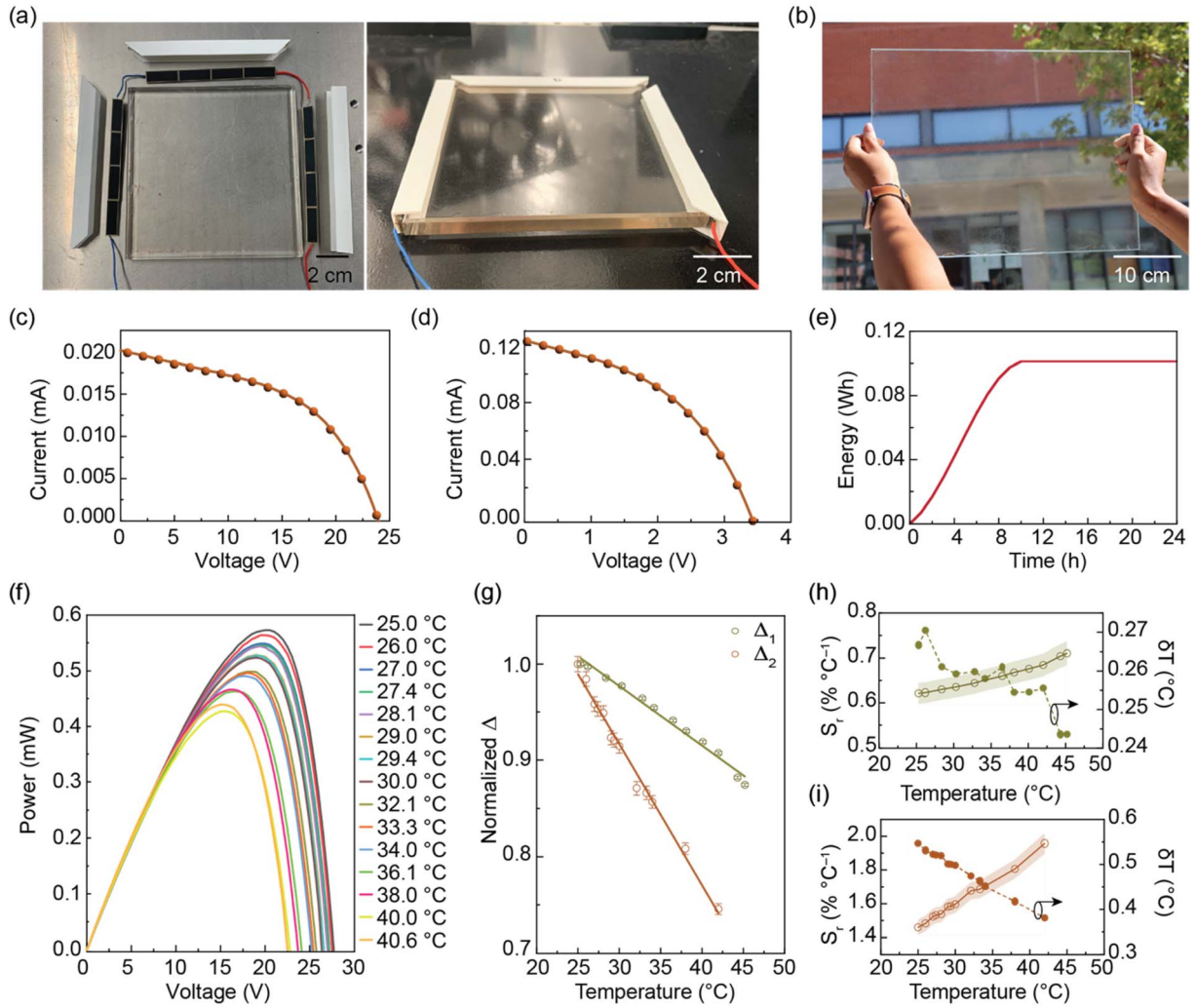

Fig. 5 Photographs of (a) the prototype assembly with a 12 c-Si solar cell array and PVC frame and (b) of the fabricated large-area prototype (0.1 m^2 surface area) under outdoor sunlight conditions. *I–V* curves of the PV cells coupled to the edges of the (c) 10.5 × 10.5 × 0.8 cm^3 and (d) 38 × 28 × 0.8 cm^3 BChl/SEBS LSC prototypes. (e) Energy generated by the 10.5 × 10.5 × 0.8 cm^3 LSC device. (f) Power–voltage curves generated by the LSC edge-coupled PV cells as a function of the temperature. (g) Temperature calibration curve with the thermometric parameters Δ_1 and Δ_2 (the lines are the best linear fit with $r^2 > 0.99$) and relative thermal sensitivity S_r and temperature uncertainty δT calculated for (h) Δ_1 and (i) Δ_2. The lines in (h) and (i) are visual guides.

(Fig. 5a) which harvested the BChl/SEBS emission guided and concentrated along the edges of the substrate. The LSC's performance was evaluated under simulated AM 1.5 G irradiation (Fig. 5c, d and S15, ESI†) and the figures of merit were estimated according to the standard definitions of external photon efficiency (η_{ext}) and device efficiency (η_{dev}) recently reported:[75,76]

$$\eta_{ext} = \frac{\text{no. of edge} - \text{emitted photons}}{\text{no. of total incident photons}} \quad (4)$$

$$\eta_{dev} = \frac{\text{power from edge} - \text{coupled PV cell}}{\text{incident optical power}} \quad (5)$$

resulting in $\eta_{ext} = 1.00 \pm 0.02\%$ and $\eta_{dev} = 0.04 \pm 0.01\%$, respectively (ESI† for details).

These values are similar to those reported for NIR-emitting synthetic dyes[8,31–34] and, although lower than those reported for QDs NIR-emitting LSCs with similar emission spectral range,[8,26,29,30] this represents the first ever reported LSC based on a NIR-emitting natural optically active centers, serving as a proof of concept and paving the way for further research and innovation in this direction. The devices' output energy was also estimated considering an initial 24 hour period with a maximum recorded solar radiation of 1000 W m^{-2} after four hours from the start of the test (Fig. 5e).

Additionally, the scale-up of this nature-based NIR LSC was proven by fabricating a large area LSC by coating a 38 × 28 × 0.8 cm^3 glass substrate with the BChl/SEBS material, resulting in a transparent glass that could be used as a window in real world applications (Fig. 5b). The haze of the coating was quantified by measuring total and diffuse reflectance, yielding values between ~0.10 and ~0.35 across the visible spectrum (Fig. S16, ESI†). This haze is attributed to the unoptimized

Table 2 Calibration curve slope (°C^{-1}), thermal sensitivity (% °C^{-1}) and temperature uncertainty (°C) of the Δ_{1-2} thermometric parameters. The thermometric parameters of temperature sensors based on LSCs under AM 1.5 G radiation are also shown

	Optical centre	λ_p	Δ	Slope (°C^{-1})	S_r (% °C^{-1})	δT (°C)
Spectrometer	BChl [this work]	770	Δ_1[a]	$(-6.2 \pm 0.2) \times 10^{-3}$	0.71 ± 0.03	0.3
	eGFP[13]	510		$(-1.23 \pm 0.05) \times 10^{-3}$	1.13 ± 0.01	0.9
	APC[13]	665		$(-0.9 \pm 0.1) \times 10^{-3}$	0.91 ± 0.02	1.3
	CDs[14]	535		$(2.98 \pm 0.04) \times 10^{-3}$	0.33 ± 0.01	1
PV cell	BChl [this work]	770	Δ_2	$(-1.46 \pm 0.04) \times 10^{-2}$	1.96 ± 0.06	0.4
	CDs[14]	535		$(-8.60 \pm 0.02) \times 10^{-2}$	1.03 ± 0.03	0.4
	eGFP[13]	510	$\Delta \equiv \frac{V_{oc1}}{V_{oc}}$	$(-1.2 \pm 0.4) \times 10^{-2}$	1.23 ± 0.03	0.02
	Eu^{3+} (ref. 15)	612		$(-2.9 \pm 0.2) \times 10^{-3}$	0.29 ± 0.02	0.3

[a] Here are included all examples in which the thermometric parameter is based on the ratio between integrated areas of defined regions of the emission spectra. V_{oc1} – open-circuit voltage values measured at the PV cell attached to the LSC, when coupled to wavelength-discriminating filter; V_{oc} – open-circuit voltage values measured at the PV cell directly attached to the LSC.

deposition method rather than the SEBS matrix or dye clusters, as confirmed by the AVT measurements and the assessment of transmitted light quality (Table 1), which indicate minimal distortion. While some haze is present, it does not significantly affect optical clarity and may even be advantageous for LSC performance. Moderate light scattering can enhance light trapping and total internal reflection within the waveguide, improving photon guidance toward the solar cells at the edges while maintaining sufficient transparency.[77,78]

BChl/SEBS-based LSC as a temperature sensor

The emission spectra of the LSC based on BChl/SEBS under simulated solar irradiation show the two main bands of BChl emission as described above (Fig. S17a, ESI†), confirming its ability to efficiently absorb and convert solar radiation. Moreover, the relative intensity of the aforementioned bands is temperature-dependent (Fig. S17a, ESI†). Thus, we propose the definition of the following ratiometric thermometric parameter:[13]

$$\Delta_1 \equiv \frac{S_2}{S_1} \quad (6)$$

where S_1 and S_2 are the partial spectral integrated intensity in the 750–850 nm and 650–750 nm spectral ranges (shadowed areas in Fig. S17a, ESI†), respectively, which comprises both emission bands of BChl (Fig. 5a). The ratiometric thermometric parameter is independent of solar irradiance fluctuations during a diurnal cycle and reveals a linear dependence on the temperature with a maximum S_r value of $0.71 \pm 0.03\%$ °C^{-1}, with δT of 0.3 °C granting the possibility to accurately sense temperature[52] (Table 2, Fig. 5g and h).

We note that although S_r is commonly used as a figure of merit to compare different thermometers, it depends on experimental conditions (*e.g.* emission spectra resolution) and the sample characteristics, such as concentration and media.[58] Nonetheless, the values here reported are larger than those reported for an environmentally-friendly nature-based thermometer based on enhanced green fluorescent protein (eGFP) (0.23% °C^{-1})[79] and for the one based on carbon dots (0.3% °C^{-1})[14] (Table 2).

The temperature-dependent photoluminescence features of the BChl/SEBS also result in a variation in the optical and electrical performances of the LSC under the solar simulator irradiation (Fig. S17b, ESI†). This analysis showed that the generated electrical power (P_{out}) decreases as the temperature is elevated (Fig. 5f), allowing the definition of the thermometric parameter:

$$\Delta_2 \equiv \frac{P_{out}}{P_0} \quad (7)$$

where P_0 is the reference power value measured at room temperature (25 °C). The thermometric parameter follows a linear dependence with temperature (Fig. 5g and Table 2), showing a maximum S_r value of $1.96 \pm 0.06\%$ °C^{-1}, with δT of 0.4 °C (Table 2 and Fig. 5i). From the results presented above, it is worth noting that temperature affects two distinct parameters in the same device: the emission intensity and P_{out}. Given that both established thermometric parameters Δ_1 and Δ_2 exhibit linear dependencies, they can be effectively employed for multiparametric thermal readings, as they offer two distinct pathways for temperature determination (a concept known as multi-readout).[52] Considering the typical energy consumption of an IoT platform for data transmission (Fig. S18, ESI†),[15] our findings suggest that the implementation of a system capable of collecting, transmitting, and converting data to temperature for real-time user visualization on an online platform can be achieved without the need for an additional external power supply.

Conclusions

Luminescent solar concentrators (LSCs) offer seamless integration of photovoltaics within buildings, preserving aesthetics and indoor light quality. This study presents large-area LSC prototypes utilizing nature-based NIR-emitting molecules—specifically, bacteriochlorophyll embedded within a styrene–ethylene–butylene–styrene (SEBS) matrix. Optical and power conversion efficiencies of 1.0% and 0.04%, respectively, were achieved, highlighting the potential of nature-based LSCs for promoting more sustainable methodologies in device fabrication.

This work serves as a proof of concept, emphasizing the need to explore alternatives to conventional luminophores, which have been widely studied and applied. While naturally derived luminophores may not yet be the most cost-effective option for highly efficient LSCs, our primary goal was to demonstrate the potential of sustainable materials, paving the way for further research and innovation. We acknowledge that further improvements in energy efficiency can be achieved through optimization strategies, and future work will focus on refining the optical design *via* surface patterning, enhancing PV cell coupling techniques, and exploring energy recovery mechanisms such as reflective coatings and secondary optical elements to minimize losses and maximize performance.

Beyond its photovoltaic function, the temperature-dependent emission properties of the material have enabled the establishment of two distinct thermometric parameters, derived from its emission characteristics and the electrical power generated by edge-mounted photovoltaic cells integrated into the LSC. The remarkable performance is underscored by relative sensitivity values reaching up to 1.96% $°C^{-1}$. In a significant advancement, the prototype has been successfully scaled up to cover an active area of 0.1 m^2. This achievement marks a milestone as the first large-area LSC employing NIR emission centers derived from natural materials, offering immense potential for applications in both energy harvesting and precise temperature sensing.

Data availability

The data supporting this article have been included as part of the ESI.†

Author contributions

RASF, PSA and VS conceived the idea of the experiment; SFHC, BPF and GF took experimental data regarding the physics characterization. The bacteriochlorophyll production was accomplished by JCF and JA. The bacteriochlorophyll extraction process, including their concentration and purification, was developed, and optimized by BMCV, LSC, LMSM, SPMV. VS performed its incorporation on SEBS matrix. VS and LF performed the structural characterization and analysis. The UHPLC-MS analysis was performed by DCGAP. All authors have read and contributed to writing, besides agreeing to the final version of the manuscript.

Conflicts of interest

There are no conflicts to declare.

Acknowledgements

This work was developed within the scope of the projects CICECO – Aveiro Institute of Materials, UIDB/50011/2020 (**https://doi.org/10.54499/UIDB/50011/2020**), UIDP/50011/2020 (**https://doi.org/10.54499/UIDP/50011/2020**) and LA/P/0006/2020 (**https://doi.org/10.54499/LA/P/0006/2020**) and Instituto de Telecomunicações, UIDB/50008/2020 (**https://doi.org/10.54499/UIDB/50008/2020**), UIDP/50008/2020 (**https://doi.org/10.54499/UIDP/50008/2020**) and LA/P/0109/2020 (**https://doi.org/10.54499/LA/P/0109/2020**), Applied Molecular Biosciences Unit – UCIBIO, UIDP/04378/2020 (**https://doi.org/10.54499/UIDP/04378/2020**) and UIDB/04378/2020 (**https://doi.org/10.54499/UIDB/04378/2020**), Associate Laboratory Institute for Health and Bioeconomy – i4HB, LA/P/0140/2020 (**https://doi.org/10.54499/LA/P/0140/2020**), LAQV-Tecnologia e Processos Limpos (UID/QUI/50006/2019) and projects PLANETa (CENTRO-01-0145-FEDER-181242), and SOLPOWINS – Solar-Powered Smart Windows for Sustainable Buildings (PTDC/CTM-REF/4304/2020) financed by national funds through the FCT/MEC (PIDDAC), and when appropriate co-financed by FEDER under the PT2020 Partnership through European Regional Development Fund (ERDF) in the frame of Operational Competitiveness and Internationalization Programme (POCI). S. F. H. C. thanks FCT (2022.03740.CEECIND) and European Space Agency (ESA STAR AO 2-1790). B. M. C. V. and G. F. thank FCT for the doctoral grants (2022.13816.BD and 2023.00526.BDANA, respectively).

References

1 R. A. S. Ferreira, S. F. H. Correia, A. Monguzzi, X. Liu and F. Meinardi, *Mater. Today*, 2020, **33**, 105–121.
2 T. A. de Bruin and W. G. J. H. M. van Sark, *Adv. Photon. Res.*, 2025, **6**, 2400068.
3 Y. M. Zhao and R. R. Lunt, *Adv. Energy Mater.*, 2013, **3**, 1143–1148.
4 Y. M. Zhao, G. A. Meek, B. G. Levine and R. R. Lunt, *Adv. Opt. Mater.*, 2014, **2**, 606–611.
5 E. Dumas, C. Gao, D. Suffern, S. E. Bradforth, N. M. Dimitrijevic and J. L. Nadeau, *Environ. Sci. Technol.*, 2010, **44**, 1464–1470.
6 F. Meinardi, H. McDaniel, F. Carulli, A. Colombo, K. A. Velizhanin, N. S. Makarov, R. Simonutti, V. I. Klimov and S. Brovellii, *Nat. Nanotechnol.*, 2015, **10**, 878–885.
7 *Transforming our World: The 2030 Agenda for Sustainable Development*, **https://sdgs.un.org/2030agenda**, accessed May 2nd, 2019.
8 R. A. S. Ferreira, S. F. H. Correia, P. Geogieva, L. Fu, M. Antunes and P. S. André, *Sci. Data*, 2024, **11**, 50.
9 M. A. Hernández-Rodríguez, S. F. H. Correia, R. A. S. Ferreira and L. D. Carlos, *J. Appl. Phys.*, 2022, **131**, 140901.
10 C. L. Mulder, L. Theogarajan, M. Currie, J. K. Mapel, M. A. Baldo, M. Vaughn, P. Willard, B. D. Bruce, M. W. Moss, C. E. McLain and J. P. Morseman, *Adv. Mater.*, 2009, **21**, 3181–3185.
11 R. Bose, M. Gonzalez, P. Jenkins, R. Walters, J. Morseman, M. Moss, C. McLain, P. Linsert, A. Buchtemann, A. J. Chatten and K. W. J. Barnham, *Presented in Part at the 35th IEEE Photovoltaic Specialists Conference*, Honolulu, USA, 20–25 June, 2010.
12 S. Sadeghi, R. Melikov, H. B. Jalali, O. Karatum, S. B. Srivastava, D. Conkar, E. N. Firat-Karalar and

S. Nizamoglu, *ACS Appl. Mater. Interfaces*, 2019, **11**, 8710–8716.
13 S. F. H. Correia, A. R. N. Bastos, M. Martins, I. P. E. Macário, T. Veloso, J. L. Pereira, J. A. P. Coutinho, S. P. M. Ventura, P. S. André and R. A. S. Ferreira, *Adv. Sci.*, 2022, **9**, 2104801.
14 S. F. H. Correia, L. Fu, L. M. S. Dias, R. F. P. Pereira, V. de Zea Bermudez, P. S. André and R. A. S. Ferreira, *Nanoscale Adv.*, 2023, **5**, 3428–3438.
15 G. Figueiredo, S. F. H. Correia, B. P. Falcão, V. Sencadas, L. Fu, P. S. André and R. A. S. Ferreira, *Adv. Sci.*, 2024, **11**, 2400540.
16 F. Meinardi, F. Bruni, C. Castellan, M. Meucci, A. M. Umair, M. La Rosa, J. Catani and S. Brovelli, *Adv. Energy Mater.*, 2024, **14**, 2304006.
17 M. Kennedy, S. J. McCormack, J. Doran and B. Norton, *Sol. Energy*, 2009, **83**, 978–981.
18 S. R. Wilton, M. R. Fetterman, J. J. Low, G. J. You, Z. Y. Jiang and J. Xu, *Opt. Express*, 2014, **22**, A35–A43.
19 L. R. Bradshaw, K. E. Knowles, S. McDowall and D. R. Gamelin, *Nano Lett.*, 2015, **15**, 1315–1323.
20 X. M. Hu, R. D. Kang, Y. Y. Zhang, L. G. Deng, H. Z. Zhong, B. S. Zou and L. J. Shi, *Opt. Express*, 2015, **23**, A858–A867.
21 K. E. Knowles, T. B. Kilburn, D. G. Alzate, S. McDowall and D. R. Gamelin, *Chem. Commun.*, 2015, **51**, 9129–9132.
22 R. H. Inman, G. V. Shcherbatyuk, D. Medvedko, A. Gopinathan and S. Ghosh, *Opt. Express*, 2011, **19**, 24308–24313.
23 G. V. Shcherbatyuk, R. H. Inman, C. Wang, R. Winston and S. Ghosh, *Appl. Phys. Lett.*, 2010, **96**, 191901.
24 D. L. Waldron, A. Preske, J. M. Zawodny, T. D. Krauss and M. C. Gupta, *Nanotechnology*, 2017, **28**, 095205.
25 Y. Zhou, D. Benetti, Z. Fan, H. Zhao, D. Ma, A. O. Govorov, A. Vomiero and F. Rosei, *Adv. Energy Mater.*, 2016, **6**, 1501913.
26 X. Liu, B. Luo, J. Liu, D. Jing, D. Benetti and F. Rosei, *J. Mater. Chem. A*, 2020, **8**, 1787–1798.
27 A. Anand, M. L. Zaffalon, G. Gariano, A. Camellini, M. Gandini, R. Brescia, C. Capitani, F. Bruni, V. Pinchetti, M. Zavelani-Rossi, F. Meinardi, S. A. Crooker and S. Brovelli, *Adv. Funct. Mater.*, 2020, **30**, 1906629.
28 M. R. Bergren, N. S. Makarov, K. Ramasamy, A. Jackson, R. Gughelmetti and H. McDaniel, *ACS Energy Lett.*, 2018, **3**, 520–525.
29 M. B. Zhu, Y. X. Li, S. Q. Tian, Y. Xie, X. J. Zhao and X. Gong, *J. Colloid Interface Sci.*, 2019, **534**, 509–517.
30 J. Huang, J. J. Zhou, T. Haraldsson, A. Clemments, M. Fujii, H. Sugimoto, B. Xu and I. Sychugov, *Sol. RRL*, 2020, **4**, 2000195.
31 V. Sholin, J. D. Olson and S. A. Carter, *J. Appl. Phys.*, 2007, **101**, 123114.
32 C. H. Yang, M. Moemeni, M. Bates, W. Sheng, B. Borhan and R. R. Lunt, *Adv. Opt. Mater.*, 2020, **8**, 1901536.
33 C. C. Yang, J. Zhang, W. T. Peng, W. Sheng, D. Y. Liu, P. S. Kuttipillai, M. Young, M. R. Donahue, B. G. Levine, B. Borhan and R. R. Lunt, *Sci. Rep.*, 2018, **8**, 16359.
34 R. Rondão, A. R. Frias, S. F. H. Correia, L. S. Fu, V. de Zea Bermudez, P. S. André, R. A. S. Ferreira and L. D. Carlos, *ACS Appl. Mater. Interfaces*, 2017, **9**, 12540–12546.
35 R. Mazzaro, A. Gradone, S. Angelon, G. Morselli, P. G. Cozzi, F. Romano, A. Vomiero and P. Ceroni, *ACS Photonics*, 2019, **6**, 2303–2311.
36 A. R. Frias, S. F. H. Correia, M. Martins, S. P. M. Ventura, E. Pecoraro, S. L. Ribeiro, P. S. Andre, R. A. S. Ferreira, J. A. P. Coutinho and L. D. Carlos, *Adv. Sustain. Syst.*, 2019, **3**, 1800134.
37 A. R. Frias, E. Pecoraro, S. F. H. Correia, L. M. G. Minas, A. R. Bastos, S. Garcia-Revilla, R. Balda, S. J. L. Ribeiro, P. S. Andre, L. D. Carlos and R. A. S. Ferreira, *J. Mater. Chem. A*, 2018, **6**, 8712–8723.
38 C. P. A. Carlos, S. F. H. Correia, M. Martins, O. A. Savchuk, J. A. P. Coutinho, P. S. André, J. B. Nieder, S. P. M. Ventura and R. A. S. Ferreira, *Green Chem.*, 2020, **22**, 4943–4951.
39 F. Chemat, M. Abert-Vian, A. S. Fabiano-Tixier, J. Strube, L. Uhlenbrock, V. Gunjevic and G. Cravotto, *TrAC, Trends Anal. Chem.*, 2019, **118**, 248–263.
40 T. Zhou, A. Zhang, C. S. Zhao, H. W. Liang, Z. Y. Wu and J. K. Xia, *Macromolecules*, 2007, **40**, 9009–9017.
41 J. Rieger, *J. Therm. Anal.*, 1996, **46**, 965–972.
42 Q. Beuguel, E. Kirillov, J. F. Carpentier and S. M. Guillaume, *ACS Appl. Polym. Mater.*, 2022, **4**, 2251–2255.
43 C. C. White, K. T. Tan, D. L. Hunston, T. Nguyen, D. J. Benatti, D. Stanley and J. W. Chin, *Polym. Degrad. Stab.*, 2011, **96**, 1104–1110.
44 A. K. Pal, A. K. Mohanty and M. Misra, *RSC Adv.*, 2021, **11**, 36398–36438.
45 Y. Zhao, A. W. Dunn and D. L. Shi, *MRS Commun.*, 2019, **9**, 675–681.
46 B. Grimm, R. J. Porra, W. Rüdiger and H. Scheer, *Chlorophylls and Bacteriochlorophylls: Biochemistry, Biophysics, Functions and Applications*, Springer, Dordrecht, 2006.
47 A. W. D. Larkum, R. J. Ritchie and J. A. Raven, *Photosynthetica*, 2018, **56**, 11–43.
48 R. K. Clayton, *Photochem. Photobiol.*, 1966, **5**, 669–677.
49 E. Siefert, R. L. Irgens and N. Pfennig, *Appl. Environ. Microbiol.*, 1978, **35**, 38–44.
50 R. U. Meckenstock, R. A. Brunisholz and H. Zuber, *FEBS Lett.*, 1992, **311**, 128–134.
51 J. F. C. B. Ramalho, A. N. C. Neto, L. D. Carlos, P. S. André and R. A. S. Ferreira, in *Handbook on the Physics and Chemistry of Rare Earths*, ed. J.-C. Bünzli and V. K. Pecharsky, Elsevier Science, B. V., Amsterdam, 2022, ch. 324, vol. 61, pp. 31–128.
52 J. F. C. B. Ramalho, L. D. Carlos, P. S. André and R. A. S. Ferreira, *Adv. Photonics Res.*, 2021, **6**, 2000211.
53 M. Martins, C. M. Albuquerque, C. F. Pereira, J. A. P. Coutinho, M. G. P. M. S. Neves, D. C. G. A. Pinto, M. A. F. Faustino and S. P. M. Ventura, *ACS Sustain. Chem. Eng.*, 2021, **9**, 1772–1780.
54 M. Martins, A. P. M. Fernandes, M. A. Torres-Acosta, P. N. Collen, M. H. Abreu and S. P. M. Ventura, *Sep. Purif. Technol.*, 2021, **254**, 117589.

55 T. E. Sintra, S. S. Bagagem, F. G. Ahsaie, A. Fernandes, M. Martins, I. P. E. Macario, J. L. Pereira, F. J. M. Goncalves, G. Pazuki, J. A. P. Coutinho and S. P. M. Ventura, *Sep. Purif. Technol.*, 2021, **255**, 117538.
56 C. A. S. Ruiz, M. Martins, J. A. P. Coutinho, R. H. Wijffels, M. H. M. Eppink, C. van den Berg and S. P. M. Ventura, *Chem. Eng. J.*, 2020, **399**, 125683.
57 S. A. Wade, S. F. Collins and G. W. Baxter, *J. Appl. Phys.*, 2003, **94**, 4743–4756.
58 C. D. S. Brites, A. Millán and L. D. Carlos, in *Handbook on the Physics and Chemistry of Rare Earths*, ed. J.-C. Bünzli and V. K. Pecharsky, Elsevier Science, B. V., Amsterdam, 2016, ch. 281, vol. 49, pp. 339–427.
59 *IXOLAR™ High Efficiency SolarBIT IXYS KXOB25-01X8F*, **https://waf-e.dubudisk.com/anysolar.dubuplus.com/techsupport@anysolar.biz/O18Adzl/DubuDisk/www/Gen2/KXOB25-01X8FDATASHEET202007.pdf**.
60 S. Pareek, N. A. Sagar, S. Sharma, V. Kumar, T. Agarwal, G. A. González-Aguilar and E. M. Yahia, in *Fruit and Vegetable Phytochemicals: Chemistry and Human Health*, ed. E. M. Yahia, John Wiley & Sons Ltd, 2nd edn, 2017, pp. 269–284, DOI: **10.1002/9781119158042.ch14**.
61 M. Martins, R. Oliveira, J. A. P. Coutinho, M. A. F. Faustino, M. G. P. M. S. Neves, D. C. G. A. Pinto and S. P. M. Ventura, *Sep. Purif. Technol.*, 2021, **255**, 117723.
62 M. Martins, C. W. Ooi, M. C. Neves, J. F. B. Pereira, J. A. P. Coutinho and S. P. M. Ventura, *J. Chem. Technol. Biotechnol.*, 2018, **93**, 1864–1870.
63 M. Kholany, P. Trebulle, M. Martins, S. P. M. Ventura, J. M. Nicaud and J. A. P. Coutinho, *J. Chem. Technol. Biotechnol.*, 2020, **95**, 1126–1134.
64 W. Mantele, A. Wollenweber, F. Rashwan, J. Heinze, E. Nabedryk, G. Berger and J. Breton, *Photochem. Photobiol.*, 1988, **47**, 451–455.
65 S. S. Kumar, P. Manoj and P. Giridhar, *J. Food Sci. Technol.*, 2015, **52**, 8131–8139.
66 V. Benedetti, M. Scatto, M. Baratieri and P. Riello, *Waste Biomass Valorization*, 2021, **12**, 3485–3496.
67 E. Alikhani, M. Mohammadi and M. Sabzi, *Polym. Bull.*, 2023, **80**, 7991–8012.
68 M. A. Paglicawan and J. R. Celorico, *Polym. Polym. Compos.*, 2021, **29**, S154–S165.
69 B. M. C. Vaz, M. Martins, L. M. D. Mesquita, M. C. Neves, A. P. M. Fernandes, D. C. G. A. Pinto, M. G. P. M. S. Neves, J. A. P. Coutinho and S. P. M. Ventura, *Chem. Eng. J.*, 2022, **428**, 131073.
70 Y. Wang, Y. Q. Liu, G. M. Xie, J. L. Chen, P. Li, Y. H. Zhang and H. R. Li, *ACS Appl. Mater. Interfaces*, 2022, **14**, 5951–5958.
71 M. L. Gómez, D. P. Fasce, R. J. J. Williams, H. A. Montejano and C. M. Previtali, *J. Polym. Sci., Part B: Polym. Phys.*, 2008, **46**, 289–296.
72 B. S. Richards and I. A. Howard, *Energy Environ. Sci.*, 2023, **16**, 3214–3239.
73 T. A. de Bruin and W. G. J. H. M. van Sark, *Front. Phys.*, 2022, **10**, 856799.
74 R. R. Lunt, *Appl. Phys. Lett.*, 2012, **101**, 043902.
75 C. C. Yang, H. A. Atwater, M. A. Baldo, D. Baran, C. J. Barile, M. C. Barr, M. Bates, M. G. Bawendi, M. R. Bergren, B. Borhan, C. J. Brabec, S. Brovelli, V. Bulovic, P. Ceroni, M. G. Debije, J. M. Delgado-Sanchez, W. J. Dong, P. M. Duxbury, R. C. Evans, S. R. Forrest, D. R. Gamelin, N. C. Giebink, X. Gong, G. Griffini, F. Guo, C. K. Herrera, A. W. Y. Ho-Baillie, R. J. Holmes, S. K. Hong, T. Kirchartz, B. G. Levine, H. B. Li, Y. L. Li, D. Y. Liu, M. A. Loi, C. K. Luscombe, N. S. Makarov, F. Mateen, R. Mazzaro, H. McDaniel, M. D. McGehee, F. Meinardi, A. Menendez-Velazquez, J. Min, D. B. Mitzi, M. Moemeni, J. H. Moon, A. Nattestad, M. K. Nazeeruddin, A. F. Nogueira, U. W. Paetzold, D. L. Patrick, A. Pucci, B. P. Rand, E. Reichmanis, B. S. Richards, J. Roncali, F. Rosei, T. W. Schmidt, F. So, C. C. Tu, A. Vahdani, W. G. J. H. M. van Sark, R. Verduzco, A. Vomiero, W. W. H. Wong, K. F. Wu, H. L. Yip, X. W. Zhang, H. G. Zhao and R. R. Lunt, *Joule*, 2022, **6**, 8–15.
76 M. G. Debije, R. C. Evans and G. Griffini, *Energy Environ. Sci.*, 2021, **14**, 293–301.
77 C. Preston, Y. L. Xu, X. G. Han, J. N. Munday and L. B. Hu, *Nano Res.*, 2013, **6**, 461–468.
78 D. B. Mahadik, R. V. Lakshmi and H. C. Barshilia, *Sol. Energy Mater. Sol. Cells*, 2015, **140**, 61–68.
79 O. A. Savchuk, O. F. Silvestre, R. M. R. Adao and J. B. Nieder, *Sci. Rep.*, 2019, **9**, 7535.